NMR IN BIOMEDICINE
NMR Biomed. (2008)
Published online in Wiley InterScience
(www.interscience.wiley.com) DOI:10.1002/nbm.1278

Assessment of blood volume, vessel size, and the expression of angiogenic factors in two rat glioma models: a longitudinal *in vivo* and *ex vivo* study

Samuel Valable,[1,2]* Benjamin Lemasson,[1,2] Régine Farion,[1,2] Marine Beaumont,[1,2] Christoph Segebarth,[1,2] Chantal Remy[1,2] and Emmanuel L. Barbier[1,2]

[1]Inserm, U836, Grenoble, France
[2]Université Joseph Fourier, Grenoble Institut des Neurosciences, UMR-S836, Grenoble, France

Received 28 September 2007; Revised 7 February 2008; Accepted 7 March 2008

ABSTRACT: Assessment of angiogenesis may help to determine tumor grade and therapy follow-up. *In vivo* imaging methods for non-invasively monitoring microvasculature evolution are therefore of major interest for tumor management. MRI evaluation of blood volume fraction (BVf) and vessel size index (VSI) was applied to assess the evolution of tumor microvasculature in two rat models of glioma (C6 and RG2). The results show that repeated MRI of BVf and VSI – which involves repeated injection of an iron-based MR contrast agent – does not affect either the physiological status of the animals or the accuracy of the MR estimates of the microvascular parameters. The MR measurements were found to correlate well with those obtained from histology. They indicate that microvascular evolution differs significantly between the two glioma models, in good agreement with expression of angiogenic factors (vascular endothelial growth factor, angiopoietin-2) and with activities of matrix metalloproteinases, also assessed in this study. These MRI methods thus provide considerable potential for assessing the response of gliomas to anti-angiogenic and anti-vascular agents, in preclinical studies as well as in the clinic. Furthermore, as differences between the fate of tumor microvasculature may underlie differences in therapeutic response, there is a need for preclinical study of several tumor models.

KEYWORDS: MRI; brain cancer; angiogenesis; rats

INTRODUCTION

Assessing angiogenesis is important when determining tumor grade and prognosis (1–3). In clinical practice, angiogenesis is assessed in terms of microvessel density as determined on surgical biopsy specimens (4). Whereas biopsies provide information only from particular regions within the tumor, the vasculature of high-grade tumors is highly heterogeneous (5). Necrotic areas exhibit sparse and degraded vessels, whereas angiogenic areas are characterized by high vessel density (6), large vessel diameters (7), and increased permeability. *In vivo* imaging methods for monitoring microvasculature non-invasively are therefore of major interest for tumor management (8). Also, as stated by Gagner *et al*. (9), there is currently a strong need for imaging and pathological surrogate markers of angiogenesis.

MRI appears to be one of the techniques best suited to providing such markers. It is already considered the method of choice for diagnosis of brain tumors, providing information about tumor size and location, extent of edema, relative blood volume fraction (BVf) and blood–brain barrier (BBB) status. The MRI method most widely used to characterize microvasculature is dynamic susceptibility contrast imaging. With this method, the first pass of an intravenously injected bolus of a gadolinium-based contrast agent is monitored (10,11). With brain tumors, the accuracy of parameters derived from dynamic susceptibility contrast MRI may be reduced because of broadening of the arterial input function and/or alteration of BBB permeability (12–14). Steady-state methods for characterizing the microvasculature are another alternative in MRI. They are based on measurement of transverse relaxation times before and after injection of an intravascular iron-based contrast agent. With both approaches (first-pass and steady-state), it is possible to obtain an estimate of BVf and information on the distribution of microvessel radii (14–21). The latter information can be expressed in terms of vessel size index

**Correspondence to:* S. Valable, C1-NAPS UMR 6232, Centre Cyceron, Bd H. Becquerel, BP 5229, 14074 Caen cedex, France.
E-mail: Samvalable@hotmail.com
Contract/grant sponsors: La Ligue Contre le Cancer; Association pour la Recherche sur le Cancer; Institut National du Cancer; Programme Interdisciplinaire Imagerie du Petit Animal; Région Rhône-Alpes; Cancéropôle Lyon Auvergne Rhône-Alpes.

Abbreviations used: ADC, apparent coefficient diffusion; Ang-2, angiopoietin-2; BBB, blood–brain barrier; BVf, blood volume fraction; DCE, dynamic contrast-enhanced; HE, hematoxylin/eosin; MMP, matrix metalloproteinase; PBS, phosphate-buffered saline; ROI, region of interest; TBS, Tris-buffered saline; VEGF, vascular endothelial growth factor; VSI, vessel size index.

(VSI, in μm) (16,19,20). MRI mapping of VSI has been validated in various animal models (16,19,22). In humans, VSI and BVf have been mapped using gadolinium chelates rather than iron-based contrast agents (14,15, 20,23).

As there is no need for high temporal resolution with steady-state MRI methods, BVf and VSI maps can be obtained with high spatial resolution. This renders these methods particularly useful for characterizing microvasculature during tumor growth and assessing the efficiency of anti-angiogenic and/or anti-vascular therapies.

The response to a particular treatment varies between animal models (24). Histological findings suggests that structural and functional specificities of microvasculature may underlie these different therapeutic responses. To our knowledge, there have been no *in vivo* studies on microvasculature evolution in two different orthotopically implanted intracerebral glioma models as assessed by longitudinal follow-up of the same animals.

In designing this study, we had several objectives. The first was to verify the feasibility of repeated MRI mapping of BVf (BVf_{MRI}) and VSI (VSI_{MRI}) on the same animal. The second was to compare *in vivo* BVf_{MRI} and VSI_{MRI} results with the corresponding *ex vivo* histochemistry measurements of the vascular bed (BVf_{histo} and VSI_{histo}). The third objective was to characterize microvasculature evolution during the development of C6 and RG2 gliomas. The two models exhibit different degrees of aggressiveness, and we expected therefore that they would show specific types of microvascular evolution. Our final objective was to determine whether these differences – if any – would be reflected in the expression of vascular endothelial growth factor (VEGF) and angiopoietin-2 (Ang-2), and in the activity of matrix metalloproteinase (MMP)-2 and MMP-9.

METHODS

Animal manipulation

The study design was approved by the local committee for animal care and use (approval 081). Experiments were performed under permits nos 380508, A3851610004 and B3851610003 from the French Ministry of Agriculture. All experiments were performed under anesthesia: 5% isoflurane for induction, 2% for maintenance in 70% air/30% oxygen. Rectal temperature was maintained at $37.0 \pm 0.5^{\circ}C$ throughout the experiments.

Implantation of tumor cells

Male Wistar (175–200 g, $n = 27$) and Fischer 344 (150–175 g, $n = 26$) rats were used for the high-grade glioma models C6 and RG2, respectively. Cell suspensions [1×10^5 C6 cells (ATCC, CCL-107); 5×10^3 RG2 cells (ATCC, CRL-223)] were injected into the right striatum as described (25). The C6 cell line was produced by repeated administration of *N*-methylnitrosourea to outbred Wistar rats (26). The C6 model is most commonly used in studies characterizing brain tumor biology, including angiogenesis [for a review, see Refs (24) and (27)]. The mean survival time after intracerebral implantation of 10^5 cells is 28 ± 5 days. The tumor histopathology of the C6 rat glioma has been classified as astrocytoma (24).

The RG2 cell line was obtained from a tumor developed in the progeny of female Fischer 344 rats, which were injected with *N*-ethyl-*N*-nitrosourea during gestation (28). The mean survival time after intracerebral implantation of 5×10^3 cells is 22 ± 3 days. In displaying an invasive growth pattern, in being refractory to all therapeutic modalities, and in being non-immunogenic in a syngeneic host, the RG2 glioma in rat appears to be a good model for human glioblastoma (24).

For each model, a group of eight animals, called the 'longitudinal observation group', was submitted to the MRI protocol four times: 11, 15, 20, and 25 days after tumor implantation for the C6 model, and 6, 10, 14, and 18 days for the RG2 model. The last time point corresponds to about 3 days before death after the mean survival time (unpublished data). After the last MRI measurement, animals were killed for subsequent *ex vivo* experiments. At each time point, and in addition to the eight animals already mentioned, four animals were submitted to MRI and then killed for *ex vivo* experiments. This group of 16 animals (four time points, four animals/time point) forms the 'single-time observation group'.

Separate experiments were performed on the remaining three C6-bearing and two RG2-bearing animals to evaluate the amount of contrast agent that extravasates during MRI data acquisition.

In vivo MRI experiments

Experiments were performed on a horizontal 2.35 T (40 cm-diameter) magnet equipped with actively shielded gradient coils (Magnex Scientific Ltd, Oxford, UK) and interfaced to a SMIS console (SMIS Ltd, Guildford, UK).

After anesthesia, a catheter was inserted into the tail vein, and 200 μL plasma was sampled (plasma 'before injection').

T_1-weighted anatomical images were acquired using a 3D-MDEFT sequence (29): voxel size $= 333 \times 333 \times 333\ \mu m^3$, inversion time $= 605$ ms, alpha $= 22^{\circ}$, $TR/TE = 15/5$ ms. To enable mapping of the apparent diffusion coefficient (ADC) of water, three spin-echo images diffusion-weighted in the three principal directions of the gradient system, with $b = 900\ s/mm^2$ and a reference image ($b \approx 0\ s/mm^2$), were acquired (voxel size $= 234 \times 454 \times 1000\ \mu m^3$). A multi gradient-echo

DOI: 10.1002/nbm

and spin-echo MRI sequence ($TR = 6$ s; seven evenly spaced gradient echoes = 6–42 ms; one spin echo = 102 ms; voxel size = $234 \times 454 \times 1000\ \mu m^3$) was acquired just before and 4 min after administration of Sinerem® via the tail vein in about 20 s (200 μmol iron/kg body weight) (Sinerem®, Guerbet SA, Roissy, France Combidex®, Advanced Magnetics, Inc, Cambridge, MA, USA). Sinerem® is a dextran-coated iron-based contrast agent ~20 nm in size with a 4.5 h plasma half-life (19). The longitudinal and transversal relaxivities of Sinerem® at 37°C and 2.35 T are $R_1 = 8\ mM^{-1}.s^{-1}$ and $R_2 = 79\ mM^{-1}.s^{-1}$, respectively (data not shown). The saturation magnetization of iron is 0.396 μT/mmol iron (16). Total MRI examination time per animal was 1 h 20 min.

At the end of the MRI experiments, 200 μL plasma 'after injection' was sampled. To estimate the amount of contrast agent that extravasates into the tumor during measurements of BVf and VSI, dynamic contrast-enhanced MRI (DCE-MRI) (30) was performed on the separate set of animals, 18 days and 14 days after C6 and RG2 cell implantation, respectively. A T_1 map was acquired using inversion recovery, spiral imaging ($TR/TE = 4400/1.6$ ms, five interleaves, 11 inversion times, voxel size = $468 \times 468 \times 2000\ \mu m^3$). T_1-weighted spiral imaging was repeated for 20 min ($TR/TE = 600/1.6$ ms, 16 interleaves, voxel size = $234 \times 234 \times 2000\ \mu m^3$, 20 s/image). After acquisition of five baseline images (i.e. 1 min 40 s after the start of imaging), Sinerem® was administered as described above.

Determination of plasma iron concentration

The plasma samples 'before injection' and 'after injection' were diluted 8 and 20 times, respectively, with saline. T_2 measurements were performed on these diluted plasma samples and on calibration samples (known concentrations of Sinerem®), using a Carr–Purcell–Meiboom–Gill sequence (400 echoes; echo spacing = 0.9 ms and 8 ms for plasma samples collected after and before injection, respectively) (31). A mono-exponential decay was fitted to the data to determine T_2. Linear fitting of the T_2 measurements led to the following calibration equation ([Fe] in μmol iron/mL, T_2 in s):

$$[\mathrm{Fe}] = 0.01056 \times (1/T_2) - 0.00024 \qquad (1)$$

Iron concentrations in plasma were eventually obtained from the T_2 values measured in plasma, using the calibration equation.

Ex vivo experiments

At the end of the MRI experiments, rats were decapitated. Brain, spleen, and liver were quickly removed, frozen in −40°C isopentane, and stored at −80°C. Brains were sliced (coronal 20 μm-thick sections) at −20°C until about half of the tumor volume had been sliced. The remainder of the brain was kept for protein analysis.

Vascular structures in brains were detected by immunohistochemistry. Sections corresponding to the largest tumor area were rehydrated in phosphate-buffered saline (PBS, 0.01 M), fixed in 4% paraformaldehyde. After saturation in PBS/0.01% Tween/3% BSA for 1 h at room temperature, a goat antibody directed against collagen IV (Southern Biotech, Birmingham, AL, USA) was incubated overnight at 4°C in PBS/0.01% Tween/1% BSA, and visualization was performed using an Alexa 546-linked donkey anti-goat IgG (Invitrogen; Fischer Scientific Bioblock, Illkirch, France). Adjacent sections were stained with hematoxylin/eosin (HE).

Iron deposits were detected using Prussian Blue staining on adjacent brain sections as well as on sections from liver and spleen. Slices were incubated with 2% potassium ferrocyanide (Perl's reagent; Sigma, Lille-Lezennes, France) in 2% HCl for 20 min, washed and counterstained with erythrosin.

Protein preparation. The second part of the brain was split into the contralateral hemisphere (c) and the ipsilateral hemisphere (i). Brain samples were homogenized in a 2:1 (v/w) ratio of lysis buffer containing Tris (50 mM), NaCl (150 mM), and 0.5% Triton X-100 (Sigma Aldrich) (32). Protein concentrations of the extracts were determined using a BCA protein assay kit (Pierce, Perbio Science France SAS, Berbière, France).

Western-blot analysis. After separation of proteins by SDS/PAGE, proteins were transferred to poly(vinylidene difluoride) membranes (GE Healthcare Bio-Sciences, Uppsala, Sweden). After saturation for 1 h in 5% (w/v) non-fat milk in Tris-buffered saline (TBS) containing 0.05% Tween 20 (T-TBS), antibodies were incubated overnight at 4°C [VEGF and Ang-2 antibodies (Upstate/Chemicon, Saint-Quentin-en-Yvelines, France); β-actin antibody (Sigma)]. After being washed in T-TBS, membranes were incubated for 1 h at room temperature with peroxidase-linked secondary antibodies, and the immunoreactive bands were visualized by enhanced chemiluminescence (GE Healthcare Bio-Sciences). The blots were then incubated in stripping buffer (62 mM Tris/HCl, pH 6.8; 2% SDS; and 100 mM β-mercaptoethanol) for 30 min at 50°C and reprobed with actin antibody.

Gelatin-based zymography

After electrophoresis, gels were washed twice with 2.5% Triton X-100. After overnight incubation at 37°C in TBS containing 5 mM $CaCl_2$, gels were stained with 0.5% Coomassie Brilliant Blue R-250 and destained with a 40% methanol/10% acetic acid solution.

DOI: 10.1002/nbm

Data processing

Determination of tumor volume. Tumor volume was determined by manually delineating the tumor on the set of T_1-weighted MR images from adjacent slices containing the lesion, by counting the voxels within the tumor boundaries, and by scaling with voxel volume.

MRI maps. All maps were computed using a program developed in-house within Matlab (The MathWorks, Inc., Natick, MA, USA). ADC was computed as the mean of the ADCs observed in the three principal directions of the gradient system. Changes in transverse relaxation rates due to Sinerem® (ΔR_2^* and ΔR_2) were obtained from gradient-echo and spin-echo signals acquired before and after injection of Sinerem® (19). The increase in the difference $\Delta\chi$ between blood and tissue susceptibilities was derived animal per animal from the difference in plasma iron concentrations measured before and after injection of Sinerem®, using the saturation magnetization of Sinerem® and the static magnetic field values (19). BVf_{MRI} maps were computed using eqn (13) from Ref. (16):

$$BVf_{MRI} = \frac{3}{4\pi}\frac{\Delta R_2^*}{\gamma\Delta\chi B_0} \tag{2}$$

where B_0 and γ represent the static magnetic field and the gyromagnetic ratio of the protons. VSI_{MRI} maps were computed using eqn (14) from Ref. (16):

$$VSI_{MRI} = 0.424\left(\frac{ADC}{\gamma\Delta\chi B_0}\right)^{1/2}\left(\frac{\Delta R_2^*}{\Delta R_2}\right)^{3/2} \tag{3}$$

Region of interest (ROI). Four ROIs (contralateral striatum, contralateral neocortex, tumor periphery, and tumor center) were delineated on the slice (ADC map for MRI and HE section for histology) containing the largest tumor area. The ROI 'center' corresponded to the region of increased ADC for the C6 model and to the region of apparently reduced ADC for the RG2 model. For the ROI 'periphery', a one voxel wide region ($\sim$250 μm) was drawn manually around the ROI 'center' (33). Voxels corresponding to cerebrospinal fluid or corpus callosum were excluded.

For histological data, the ROI 'center' corresponded to the region of high cell density, and the ROI 'periphery' was defined as a region of $\sim$300 μm width around the ROI 'center' (33).

Measurement of ADC, BVf_{MRI}, and VSI_{MRI}. Each ROI delineated on the ADC map was transferred on to the BVf_{MRI} and VSI_{MRI} maps. Within each ROI and each map, voxels were then identified for which no analysis could be performed [e.g. non-converging fit, values outside the range of validity of the method ($ADC > 3500\ \mu m^2/s$; $BVf_{MRI} > 17\%$; $VSI_{MRI} > 50\ \mu m$)], and they were excluded from the analysis. For BVf_{MRI} and VSI_{MRI}, the conditions of validity applied are those defined in Ref. (16) – our data were collected under experimental conditions identical with those in Ref. (16). For ADC, we used the ADC of pure water as the threshold. The total number of voxels, the number of excluded voxels, and the mean and standard deviations were computed for each ROI and each parameter. Rejected voxels represented 2.5% and 1.9% of the total number of voxels for the C6 and RG2 models, respectively.

DCE-MRI analysis. T_1-weighted images were converted into T_1 maps using the following relation in each voxel:

$$T_1 = -TR/\ln(1 - S/S_0) \tag{4}$$

where S represents the signal intensity in the voxel and S_0 the fully relaxed MR signal in that voxel. S_0 was computed from the baseline signal intensity (five first-time points) and from the T_1 value (T_{10}) computed from the inversion recovery data acquired before Sinerem® injection.

To analyze the decrease in voxel T_1, one first assumes that the decrease in the T_2^* signal can be neglected at the short *TE* used. Then, to estimate the upper limit of the extravascular iron concentration, one considers that all the Sinerem® has leaked into the extravascular compartment. Thus, the upper limit of the extravascular iron concentration can be estimated using:

$$[Fe] = \frac{1}{r_1}\left(\frac{1}{T_1} - \frac{1}{T_{10}}\right) \tag{5}$$

where r_1 is the relaxivity of Sinerem®.

Quantitative histology. Sections (up to three microscopic fields per ROI and per slice, three slices/animal) were digitized using a CCD camera (Olympus, Rungis, France). Collagen IV images were binarized (threshold manually defined), and vascular parameters [mean vessel density, fractional vascular surface (*VSurf*), mean vessel radius (r), and mean vessel length (h)] were obtained using ImageJ software (Rasband, W.S., ImageJ). To allow comparison between MR and histological data, VSI_{histo} was derived from two-dimensional slices as described in Ref. (19), and BVf_{histo} was computed as described in Ref. (17):

$$BVf_{histo} = \left(\frac{rh}{rh + (r+h)t}\right)[-2\ln(1 - VSurf)] \times 100 \tag{6}$$

where t is the section thickness.

Expression of the angiogenic factors. Gels were scanned and a densitometric analysis of the expression of the angiogenic factors was performed with ImageJ. For

DOI: 10.1002/nbm

the Western-blot assay, expression was normalized to that of the β-actin protein and to the expression detected for each protein in the contralateral region at the first time point.

Statistical analysis

Two-way analysis of variance followed by a *t* test *post hoc* with a Bonferroni correction were used for statistical analysis. Student *t* tests were used for neocortex/striatum comparisons. Parametric Pearson tests were used for the correlation analysis. All statistical analyses were performed with StatView SE (SAS Institute Inc, Cary, NC, USA).

RESULTS

Accuracy of the BVf_{MRI} and VSI_{MRI} measurements

Accurate BVf and VSI MRI measurements require that the iron-based contrast agent remains intravascular. DCE-MRI data indicate that the iron concentration increased slightly with time in the tumor tissue, while contralaterally it remained below the detection sensitivity of our DCE-MRI approach ($\leq 1\,\mu M$). Sixteen minutes after Sinerem® injection (corresponding to the end of MR data acquisition in the BVf_{MRI}/VSI_{MRI} experiment), the upper limits of extravascular iron concentration found in the tumor were $4\,\mu M$ and $70\,\mu M$ for the C6 and RG2 models, respectively, i.e. at most, 2% of the plasma iron concentration ($3420 \pm 970\,\mu M$, mean value for all animals across time). This mean plasma iron concentration corresponds to a mean increase, $\Delta\chi$, in plasma magnetic susceptibility of 5.6×10^{-7} cgs.

Feasibility of the longitudinal MRI follow-up

In a longitudinal study, repeated anesthesia and injections of contrast agent performed on the same animal might affect its physiological status, tumor growth, and the accuracy of the MRI measurements. No significant differences in body weight and tumor growth were observed between the 'longitudinal observation' and 'single-time observation' groups (data not shown).

In the 'longitudinal observation' group of both models, the iron concentration in the plasma, sampled before injection of Sinerem®, showed a slight increase ($+4.5 \pm 0.3\,\mu M$) between the first and second MRI sessions (Fig. 1A). Plasma iron concentration remained stable during the ensuing sessions (Fig. 1A). In brain parenchyma, T_2^* measurements before Sinerem® injection remained stable between MRI sessions for each ROI and model (Fig. 1B). With regard to histology, Prussian Blue staining showed no iron deposit in either brain tissue or tumors, at any time point for both models (Fig. 1C,a–c). In contrast, spleen sections exhibited strong iron deposits (Fig. 1C,e–f) compared with control rats, which were not injected with Sinerem® (Fig. 1C,d).

MRI data

For both models, ADC, BVf_{MRI}, and VSI_{MRI} values were not significantly different between the 'single-time observation' and 'longitudinal observation' groups, at any time point. Consequently, values for the two groups were pooled.

Contralateral data

For both models, contralateral ADC, BVf_{MRI}, and VSI_{MRI} did not vary significantly over time (Figs. 2 and 3). Values averaged over time in contralateral neocortex and striatum are summarized in Table 1. Contralateral ADC, BVf_{MRI}, and VSI_{MRI} were not significantly different between the two strains, for both ROIs. ADC and BVf_{MRI} differ significantly between neocortex and striatum in the Wistar rat. VSI_{MRI} is significantly larger in the striatum than in the neocortex for both rat strains.

Overall variability (including individual, time, and method-related variability) was ~6% for ADC, 23% for BVf_{MRI}, and 20% for VSI_{MRI}.

Tumor data

T_2-weighted images and ADC maps from the same slices (Fig. 2A,B) show that the two models evolve differently. The C6 tumor appears hyperintense on the T_2-weighted images and on the ADC maps. ADC had increased significantly in the tumor center as early as day 11 (C6 contralateral striatum, $720 \pm 50\,\mu m^2/s$; C6 center, $974 \pm 102\,\mu m^2/s$; Fig. 2A). It remained elevated in the tumor center until the end of the experiment. At the periphery of the C6 tumor, ADC did not differ from the contralateral value at any observation time. Unlike in the C6 model, ADC in the RG2 center did not vary significantly with time, remaining similar to contralateral values (Fig. 2B). At the periphery, the T_2-weighted signal and ADC values increased with time (Fig. 2B).

Tumor BVf_{MRI} and VSI_{MRI} also evolved differently in the two models. For the C6 model, BVf_{MRI} in the tumor center and periphery remained similar over time to that of the contralateral striatum (Fig. 3A), with the single exception of the periphery ROI at the last time point, day 25 (C6 contralateral striatum, $2.4 \pm 0.4\%$; C6 periphery, $4.0 \pm 1.4\%$). For the RG2 model, BVf_{MRI} had increased slightly as soon as day 10 in the center and at the periphery of the tumor (Fig. 3B). At the tumor periphery,

DOI: 10.1002/nbm

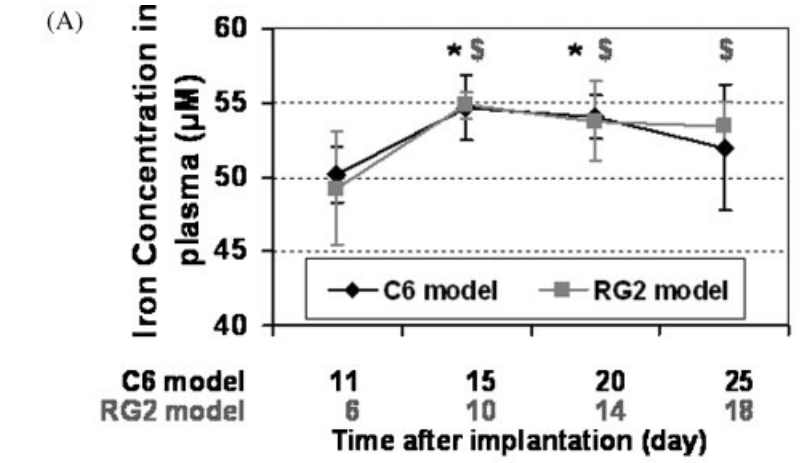

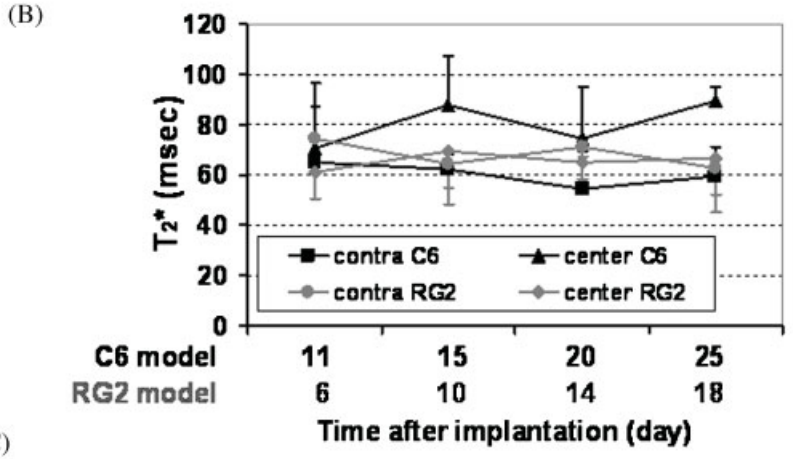

(C)

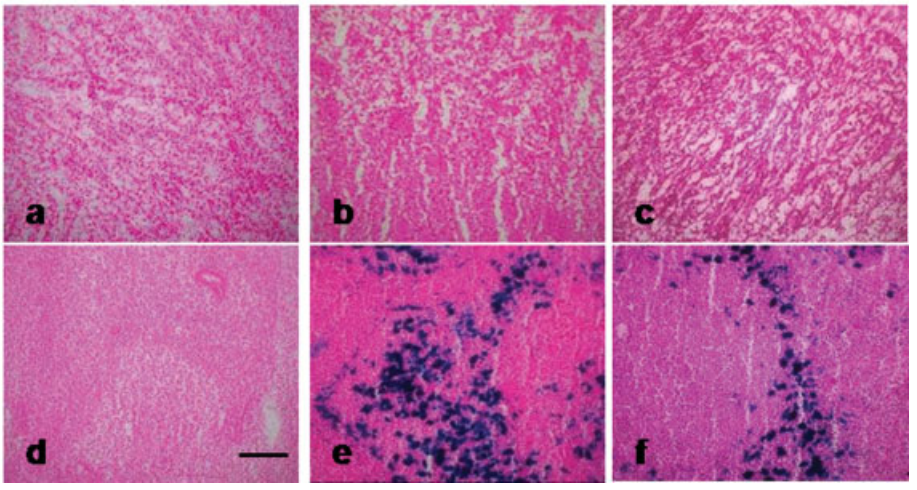

Figure 1. Sinerem® does not accumulate in plasma, brain, or glioma. (A) Iron concentration determined at each time point on plasma samples withdrawn before injection of Sinerem®. *, $, $P < 0.05$ versus the first time of analysis for the C6 model (*) and the RG2 model ($) (mean ± SD). (B) T_2^* measured in the contralateral striatum (contra) and tumor center (center) before injections of Sinerem® (mean ± SD). (C) Prussian Blue detection of iron in brain tumors (C6: a, b; RG2: c) and in spleen (d–f). (a, d) Wistar rat bearing a C6 glioma that did not receive any Sinerem®. (b, e) Wistar rat bearing a C6 glioma and (c, f) Fischer rat bearing a RG2 glioma after the fourth MRI session ('longitudinal observation' group). The sections were counterstained with erythrosin. Scale bar = 100 μm. This figure is available in colour online at www.interscience.wiley.com/journal/nbm

DOI: 10.1002/nbm

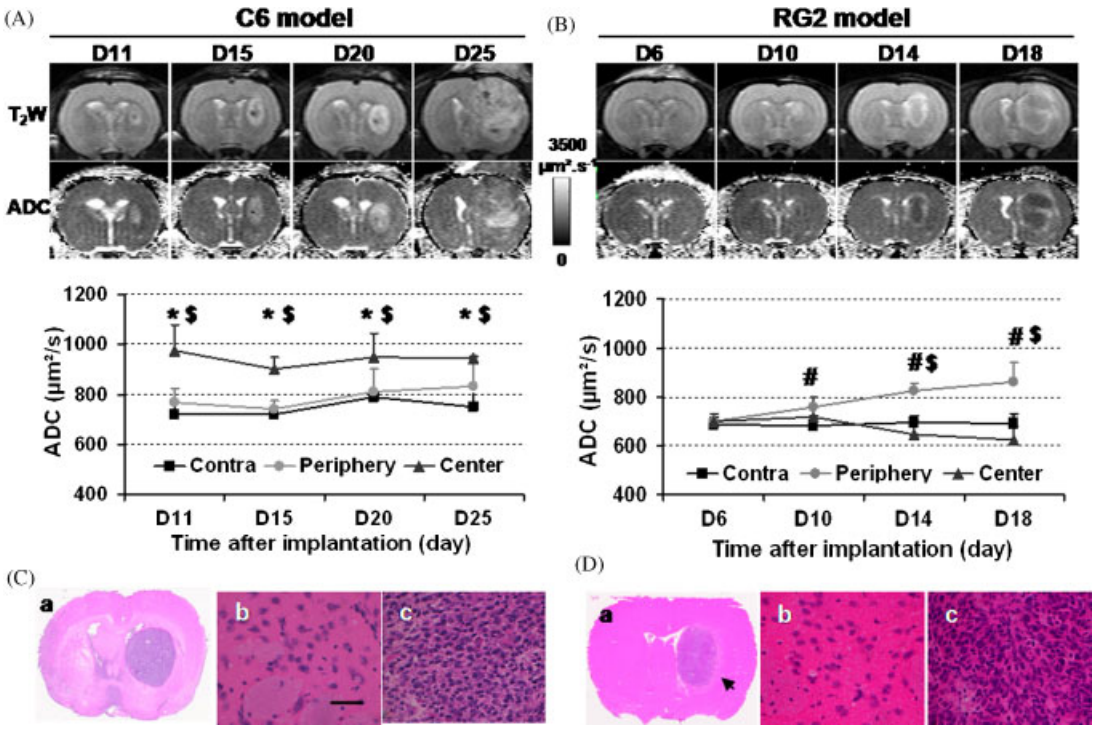

Figure 2. Evolution of tumor morphology and ADC. (A, B) T_2-weighted images and related ADC maps from a representative animal of the C6 and RG2 models. Bottom row: Corresponding evolution of ADC in the contralateral striatum, tumor periphery and tumor center. Mean ± SD. $P < 0.05$: *, tumor center versus contralateral striatum; #, tumor periphery versus contralateral striatum; $, tumor center versus tumor periphery. (C, D) HE sections for the C6 model at D20 (C,a) and for the RG2 model at D14 (D,a; arrow points to the hypostained ring corresponding to the hyperintense ring detected on the ADC map). Higher magnifications of the contralateral striatum (C,b and D,b) and tumor center (C,c and D,c). Scale bar = 100 μm. This figure is available in colour online at www.interscience.wiley.com/journal/nbm

BVf_{MRI} had further increased at day 14 to become significantly different from contralateral BVf_{MRI} (RG2 contralateral striatum, $2.5 \pm 0.6\%$; RG2 periphery, $3.4 \pm 0.6\%$) and remained stable thereafter (Fig. 3B). In the tumor center, BVf_{MRI} increased continuously until the end of the experiments (RG2 tumor center at D6, $2.5 \pm 0.6\%$, and at D18, $5.2 \pm 1.6\%$; Fig. 3B).

In the C6 model, VSI_{MRI} in the tumor was significantly higher than in the contralateral striatum as early as day 11 (C6 contralateral striatum, 5.3 ± 1.3 μm; C6 center, 8.8 ± 3.4 μm). It kept increasing until day 25 (C6 center, 19.5 ± 4.8 μm; Fig. 3A). The increase in VSI_{MRI} was less steep at the periphery than in the center (C6 periphery at D25, 11.3 ± 3.4 μm; Fig. 3A). In the RG2 model, VSI_{MRI} in the tumor center increased more slowly than in the C6 model, but it was significantly higher than contralaterally (RG2 contralateral striatum at D18, 4.6 ± 1.4 μm; RG2 center at D18, 11.0 ± 2.0 μm). At the RG2 periphery, VSI_{MRI} increased until day 14 and remained stable thereafter (Fig. 3B).

Histology

HE-stained brain sections (Fig. 2C,D) showed that, in both models, cellular density at the center of the tumor exceeded that in the contralateral striatum (Fig. 2C,b–c and 2D,b–c). No macroscopic necrotic regions were observed for the RG2 model and only at the last time point (D25) for the C6 model (results not shown). The RG2 model was also characterized by a region of low HE staining at the tumor periphery (arrow, Fig. 2D,a), corresponding to the hyperintense ring observed on the ADC maps (Fig. 2B). Finally, no hemorrhage was observed in the tumor at any time point for either model.

Immunohistology

The C6 model was characterized by a large decrease in vessel density at the tumor center (C6 contralateral striatum at D11 and D25, 297 ± 38 vessels/mm^2 and 321 ± 15 vessels/mm^2; C6 tumor center at D11 and D25, 99 ± 32 vessels/mm^2 and 70 ± 32 vessels/mm^2; Fig. 4A). In the RG2 model, vessel density was less reduced than in the C6 model (RG2 contralateral striatum at D6 and D18, 302 ± 15 vessels/mm^2 and 354 ± 40 vessels/mm^2; RG2 tumor center at D6 and D18, 254 ± 38 vessels/mm^2 and 195 ± 6 vessels/mm^2; Fig. 4B).

As to BVf_{histo}, no significant reduction was found between the tumor center and the contralateral striatum in

DOI: 10.1002/nbm

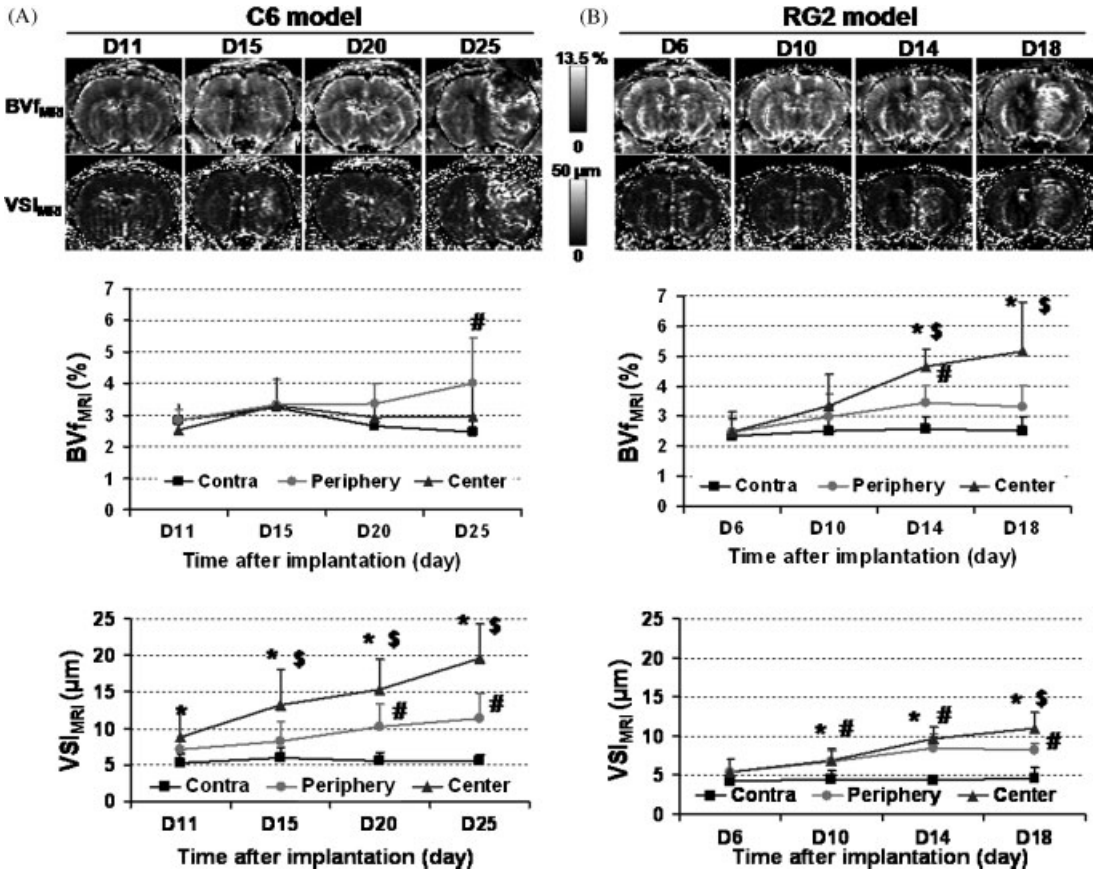

Figure 3. Evolution of BVf_{MRI} and VSI_{MRI}. (A, B) BVf_{MRI} maps and VSI_{MRI} maps from a representative animal of the C6 and RG2 models with corresponding evolutions of BVf_{MRI} and VSI_{MRI} in the contralateral striatum (contra), tumor periphery (periphery) and tumor center (center). Mean ± SD. $P < 0.05$: *, tumor center versus contralateral striatum; #, tumor periphery versus contralateral striatum; $, tumor center versus tumor periphery.

the C6 model (Fig. 4A). In the RG2 model, BVf_{histo} increased significantly with time in the tumor center (RG2 contralateral striatum at D18, $1.3 \pm 0.5\%$; RG2 tumor center at D18, $2.9 \pm 0.6\%$; Fig. 4B). After pooling of all animals and ROIs for the two models, a significant correlation between BVf_{MRI} and histological data (BVf_{histo}) was obtained ($r^2 = 0.32$; $P < 0.005$; Fig. 4C). BVf_{histo} is about three times smaller than BVf_{MRI}, however.

Table 1. Values of ADC, BVf_{MRI}, and VSI_{MRI} in the neocortex and striatum of Wistar and Fischer rats

	Wistar rats (C6 model)		Fischer rats (RG2 model)	
	Neocortex	Striatum	Neocortex	Striatum
ADC ($\mu m^2/s$)	724 ± 56	$742 \pm 69^*$	686 ± 27	688 ± 33
BVf_{MRI} (%)	3.1 ± 0.7	$2.8 \pm 0.7^*$	2.5 ± 0.6	2.5 ± 0.6
VSI_{MRI} (μm)	4.7 ± 1.2	$5.7 \pm 1.6^*$	3.7 ± 0.7	$4.4 \pm 0.9^*$

Mean 'longitudinal observation' and 'single-time observation' groups.
$^*P < 0.05$, significant difference between striatum and neocortex values.

VSI_{histo} increased continuously with time in the C6 tumor center (C6 contralateral striatum at D25, 3.7 ± 0.3 µm; C6 tumor center at D25, 9.9 ± 2.1 µm; Fig. 4A). VSI_{histo} increased less steeply with time in the RG2 tumor center than in the C6 model (RG2 contralateral striatum at D18, 3.9 ± 0.4 µm; RG2 tumor center at D18, 7.4 ± 1.3 µm; Fig. 4B). A very strong correlation between VSI_{MRI} and VSI_{histo} was found (for both models and for the three ROIs, $r^2 = 0.85$, $P < 0.0001$; Fig. 4D). VSI_{histo} is about three times smaller than VSI_{MRI}, however.

Expression of angiogenic factors

For the C6 model, expression of VEGF in the ipsilateral hemisphere (Fig. 5A) correlated well with tumor volume ($r^2 = 0.8401$). For the RG2 model, ipsilateral expression of VEGF was detected on days 14 and 18 (Fig. 5C,D). For both models, significant expression of VEGF in the contralateral hemisphere was detected only at the last time point. Ang-2 overexpression in the ipsilateral hemisphere was observed as early as day 11 for the C6 model (Fig. 5A,B), and it remained stable thereafter. For

DOI: 10.1002/nbm

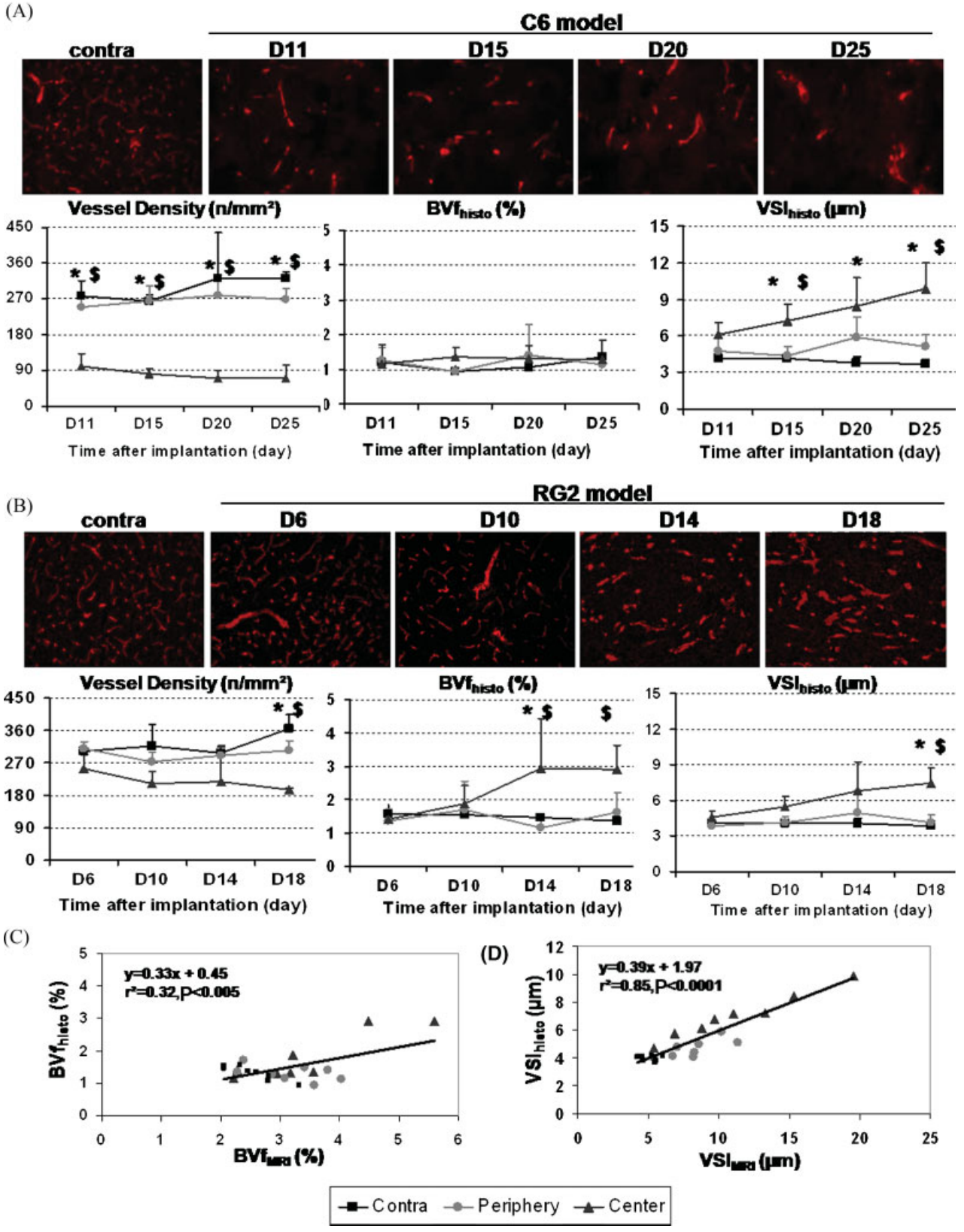

Figure 4. Evolution of vessel density, BVf_{histo}, and VSI_{histo}. (A, B) Collagen IV staining for the C6 and RG2 models with the corresponding quantitative determination of the vessel density, BVf_{histo}, and VSI_{histo} for the C6 and RG2 models in the contralateral striatum (contra), tumor periphery (periphery) and tumor center (center). Mean $\pm$ SD. $P < 0.05$: *, tumor center versus contralateral striatum; #, tumor periphery versus contralateral striatum; $, tumor center versus tumor periphery. (C) BVf_{histo} as a function of BVf_{MRI} for the different ROIs and for both models. (D) VSI_{histo} as a function of VSI_{MRI} for the different ROIs and for both models. This figure is available in colour online at www.interscience.wiley.com/journal/nbm

DOI: 10.1002/nbm

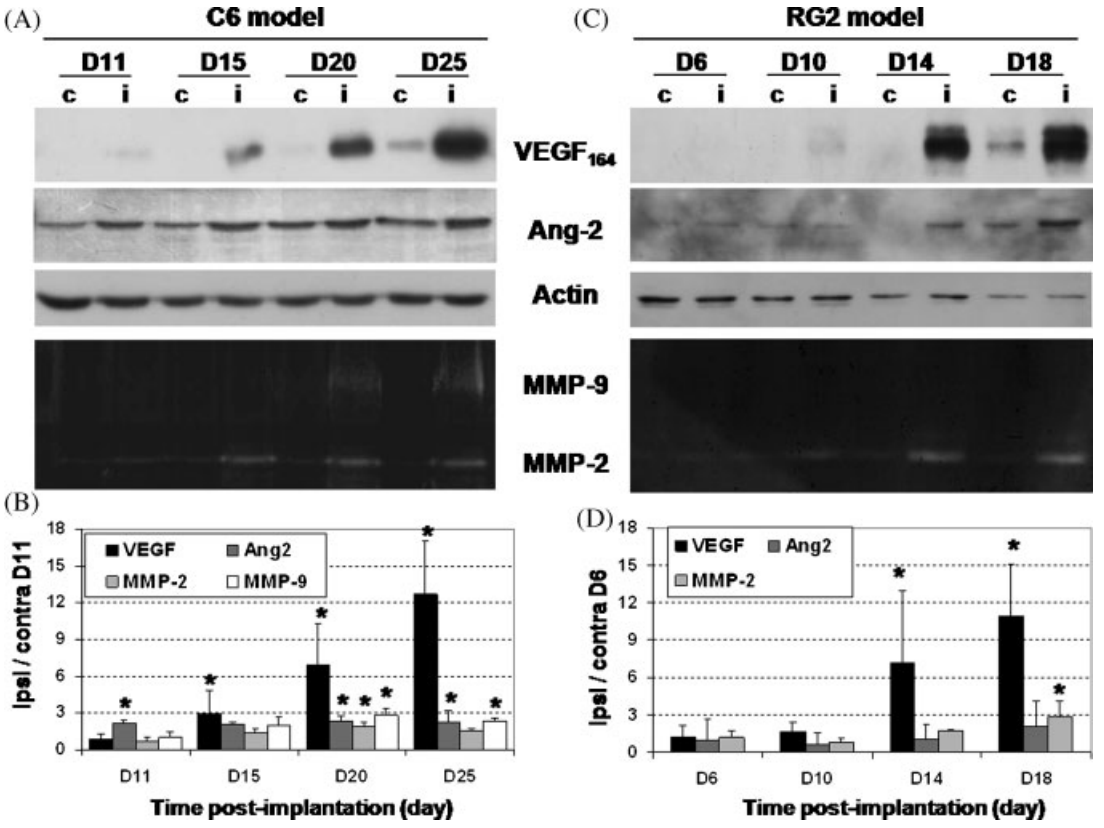

Figure 5. Evolution of the expression/activity of $VEGF_{164}$, Ang-2, MMP-2, and MMP-9. (A,C) Western-blot analysis of $VEGF_{164}$ and Ang-2 expression and zymographic analysis of MMP-2 and MMP-9 activities for the C6 and RG2 models. (B,D) Densitometric analysis of the expression/activity of $VEGF_{164}$, Ang-2, MMP-2 and MMP-9. Labels c and i stand for contralateral and ipsilateral hemispheres, respectively. Mean $\pm$ SD. *, $P < 0.05$ versus contralateral values from D11 for the C6 model or D6 for the RG2 model.

the RG2 model, ipsilateral overexpression of Ang-2 was observed on day 18 (Fig. 5C,D). MMP-2 activity appeared on day 15 for the C6 model and remained stable thereafter (Fig. 5A,B). For the RG2 model, it appeared on day 14 and increased thereafter (Fig. 5C,D). For this model, MMP-2 activity correlated with tumor volume ($r^2 = 0.8438$). Finally, MMP-9 activity was below the detection threshold in the RG2 model (Fig. 5D) at all time points, but it was detected at days 20 and 25 in the C6 model (Fig. 5A,B).

DISCUSSION

In this study, two rat glioma models were studied longitudinally. The RG2 model is more aggressive than the C6 model as judged from tumor volume doubling time of 50.7 ± 7.9 h and 87.1 ± 26.9 h, respectively. *In vivo* as well as *ex vivo* data indicate different microvasculature evolution in these two glioma models.

A primary aim of this study was to determine whether BVf and VSI MRI could be repeated over time during tumor development without affecting the physiological status of the animal and while keeping the MRI measurements stable. We therefore compared 'single-time' and 'longitudinal observation' groups in both models. Our results indicate that repeated anesthesia and injection of contrast agent had no effect on body weight, tumor volume, and MR-determined parameters. The DCE-MRI experiment, performed at days 14 and 18 for the RG2 and C6 model, respectively, showed that the extravascular concentration of Sinerem® in the tumor is, at most, 2% of the circulating concentration 20 min after injection. Furthermore, T_1-weighted images acquired at the end of the MRI protocol (i.e. 20 min after a Sinerem® injection) on two C6-bearing rats (D25) and on two RG2-bearing rats (D18) did not display signal enhancement in the tumor. Note that these data do not entirely rule out leakage of Sinerem® at some point of tumor development in certain animals from the main MRI study. However, given the measured plasma concentration of iron, the estimated upper limit of iron concentration in the extravascular space, and, most importantly, the excellent correlation between MRI and histological estimates of microvascular parameters, we are confident that, within the time frame of the MRI experiment and for the glioma models used in this study, Sinerem® can safely be considered as an intravascular contrast agent. These

DOI: 10.1002/nbm

results are in line with previously published data (21) indicating that, in the presence of a brain tumor, Sinerem®-like particles remain intravascular for at least 90 min. In plasma, a slight increase in iron concentration (~4.5 μM) was observed between the first and second MRI sessions. This increase is negligible in relation to the increase in plasma iron concentration following Sinerem® injection (~3420 μM). A massive accumulation of iron is observed in the spleen and liver of the animals, in agreement with the reported uptake of Sinerem® by Kuppfer cells (34). Within the sensitivity limits of T_2^* measurements (20% variability in our experimental conditions) and Prussian Blue staining, no iron accumulation was observed in brain parenchyma and the glioma 4 days after each Sinerem® injection. In the literature, iron accumulation has been reported 24 h after intravenous administration of Sinerem®-like particles in 9L gliosarcoma (35). Our observations, made early (20 min) and late (4 days) after Sinerem® injection, are complementary to these literature data. Taken together, our results indicate that BVf and VSI imaging repeated every 4 days over 14 days is feasible without affecting the physiological status of the rats, tumor growth, and accuracy of the MR measurements.

A second aim was to compare estimates of BVf and VSI obtained by MRI and by histology. Although the results from the two approaches show significant correlation ($P < 0.005$ and $P < 0.0001$, respectively), MRI provides estimates that are larger by a factor of ~2. Such a discrepancy has already been mentioned in Ref. (19) with regard to VSI. There are numerous sources of bias in the histological and MRI findings. First, histological estimates take into account all vessels, whereas MRI estimates rely on functional vessels only (i.e. those that are perfused by the contrast agent). Whereas freezing may induce tissue expansion, cryosectioning may induce tissue compression (36). Measuring the external diameter of objects stained with a panendothelial marker (i.e. collagen IV in the present study) yields an overestimation of the vessel diameters. The use of large dextran molecules (60–2000 kDa) or lectins coupled to a fluorescent probe to visualize *ex vivo* the perfused vessels would provide data closer to the MRI estimates (37,38). The stereological extrapolation of surface to volume parameters has limited accuracy because of the underlying assumption that vessels are perfect cylinders. Also, a 20 μm-thick histological slice does not accurately represent a 1 mm-thick MRI slice across a heterogeneous tumor. MRI estimates may be biased by the difference between the spatial configuration of real vessels (especially in a tumor) and the idealized configuration (perfect cylinders) used in modeling (39) or by macroscopic magnetic field inhomogeneities. Furthermore, as previously discussed, extravasation of Sinerem® may also yield erroneous estimates of BVf and VSI. It is hard to conclude from our results whether the 'true' values of the microvascular parameters are nearer to one or the other experimental values. The excellent correlation between parameters determined by MRI and by histology provides a strong indication that they reflect similar microvascular characteristics. Further studies are needed to gain further insights.

Additional studies should ideally include an estimate of tumor vessel permeability to gadolinium chelates, such as expressed by K_{trans} (30). Although during development and/or treatment of the tumor, K_{trans} may in certain cases correlate with BVf and VSI, there is convincing evidence that this is not generally true. For example, Leenders *et al*. (40) and Sakariassen *et al*. (41) have described tumor growth by vessel co-option (i.e. vascular dilation, increases in endothelial markers but without BBB alteration). Under such conditions, monitoring BVf and VSI rather than vascular permeability appears to be perfectly adequate for evaluating therapy. An approach in which BVf, VSI, and vascular permeability are all measured together appears to be the most satisfactory for describing a broad range of tumor types.

A third aim was to determine whether microvasculature evolves differently in two glioma models. In contralateral striatum and cortex, neither ADC, BVf, nor VSI varied with time. Contralateral values were similar in the two rat strains. The ADC values agree with previously published data (42,43). The contralateral BVf and VSI values are in agreement with those obtained by the same method in the healthy rat brain (19,44) as well as in the contralateral cortex and striatum of the C6 model (19,45).

The ADC values were found to differ greatly between the two glioma models. ADC in the tumor center was higher than contralaterally at all time points for the C6 model, whereas, for the RG2 model, it remained similar to the contralateral value. ADC may be affected by changes in cell density (or cellularity) (46,47) and by the occurrence of vasogenic edema (48). HE staining shows that cell density was increased in the tumor center of both models. The BBB permeability is known to differ between the two models (49). Therefore, development of vasogenic edema may be among the factors contributing to the differences in ADC behavior.

Regarding microvasculature, BVf increased with time in the RG2 model – in agreement with previous histological observations (50–52) – whereas it remained stable in the C6 model – in good agreement with MRI results from Tropres *et al*. (19,45) and Farrell *et al*. (53). The use of average BVf values masks the heterogeneity of the BVf, at least in the C6 model, for which, on day 25, BVf increased at the periphery of the tumor and not at the tumor center. For both models, VSI increased in the center and, to a lesser extent, at the periphery of the tumor. Previous histological studies have shown similar evolution of the mean vessel diameter in the RG2 model (51,52). Terminal VSI values in the C6 center were 1.5 to 2 times those found at the RG2 center. VSI values determined by MRI for the C6 model on day 25 are

DOI: 10.1002/nbm

identical with previously published data obtained with the same model after a similar post-implantation delay (19). The difference between healthy and tumoral tissue in VSI_{histo} values reported here (3.7 ± 0.3 vs 9.9 ± 2.1 μm, respectively) is in line with the increase in vessel diameter reported by Farrell *et al*. (53) and measured in C6 spheroids (from 3.84 ± 0.14 to 7.79 ± 0.51 μm, respectively). The stable BVf together with the VSI increase observed in the C6 model is due to a reduction in vessel density, as shown by immunohistology. Our observations are consistent with data reported by Holash *et al*. (54), indicating that initial C6 tumor growth relies on co-option of host vessels. Eventually, tumor cell proliferation decreases host vessel density and induces angiogenesis at the periphery of the tumor. The RG2 model, in contrast, is characterized by increased BVf, a smaller relative increase in VSI, and a slight reduction in vessel density.

The final question addressed was whether any differences detected between the two glioma models in the development of microvasculature can be related to the expression of the main angiogenic factors. Although expression of VEGF appears to correlate with tumoral volume, the main differences between the two models relate to Ang-2 and MMP-9. As Ang-2 is known to destabilize the microvasculature (55), its differential expression may be at the origin of the differences in VSI between the two models. Overexpression of Ang-2 was detected as early as day 11 for the C6 model. For this model, MMP-2 was also overexpressed, which may underlie the large increase in VSI detected between days 11 and 5 (56). Moreover, MMP-9 was detected ipsilaterally in the C6 model only. The early and concomitant expression of Ang-2, MMP-2 and MMP-9 could destabilize vessel walls (57) and explain the massive reduction in vessel density observed in this model.

In conclusion, this study shows that BV_{MRI} and VSI_{MRI} can be measured repeatedly over time during tumor development. MR estimates of BVf and VSI correlate well with corresponding histological estimates. Taken together, the evolution of BVf_{MRI}, VSI_{MRI}, and ADC show marked differences in the two glioma models, C6 and RG2, especially in terms of microvascular evolution. These differences, in line with the expression of angiogenic factors, suggest that these models may respond differently to particular therapies. This emphasizes the need to study several experimental tumor models in preclinical trials. Finally, BVf and VSI – as determined by MRI – appear to be potential markers for assessing non-invasively the response of gliomas to anti-angiogenic and anti-vascular agents, at the preclinical and clinical levels.

Acknowledgements

S.V. benefited from a post-doctoral grant from 'La Ligue Contre le Cancer'. We thank Guerbet for providing Sinerem®, the 'Association pour la Recherche sur le Cancer', the 'Institut National du Cancer', the 'Programme Interdisciplinaire Imagerie du Petit Animal', the 'Région Rhône-Alpes', and the 'Cancéropôle Lyon Auvergne Rhône-Alpes' for financial support.

REFERENCES

1. Burger PC, Vogel FS, Green SB, Strike TA. Glioblastoma multiforme and anaplastic astrocytoma. Pathologic criteria and prognostic implications. *Cancer* 1985; **56**(5): 1106–1111.
2. Daumas-Duport C, Tucker ML, Kolles H, Cervera P, Beuvon F, Varlet P, Udo N, Koziak M, Chodkiewicz JP. Oligodendrogliomas. Part II: a new grading system based on morphological and imaging criteria. *J. Neurooncol* 1997; **34**(1): 61–78.
3. Daumas-Duport C, Varlet P, Tucker ML, Beuvon F, Cervera P, Chodkiewicz JP. Oligodendrogliomas. Part I: patterns of growth, histological diagnosis, clinical and imaging correlations: a study of 153 cases. *J. Neurooncol* 1997; **34**(1): 37–59.
4. Takei H, Bhattacharjee MB, Rivera A, Dancer Y, Powell SZ. New immunohistochemical markers in the evaluation of central nervous system tumors: a review of 7 selected adult and pediatric brain tumors. *Arch Pathol Lab Med* 2007; **131**(2): 234–241.
5. Folkman J. Role of angiogenesis in tumor growth and metastasis. *Semin Oncol* 2002; **29**(6 Suppl 16): 15–18.
6. Carmeliet P, Jain RK. Angiogenesis in cancer and other diseases. *Nature* 2000; **407**(6801): 249–257.
7. Brown EB, Campbell RB, Tsuzuki Y, Xu L, Carmeliet P, Fukumura D, Jain RK. *In vivo* measurement of gene expression, angiogenesis and physiological function in tumors using multiphoton laser scanning microscopy. *Nat Med* 2001; **7**(7): 864–868.
8. Hou LC, Veeravagu A, Hsu AR, Tse VC. Recurrent glioblastoma multiforme: a review of natural history and management options. *Neurosurg Focus* 2006; **20**(4): E5.
9. Gagner JP, Law M, Fischer I, Newcomb EW, Zagzag D. Angiogenesis in gliomas: imaging and experimental therapeutics. *Brain Pathol* 2005; **15**(4): 342–363.
10. Barbier EL, Lamalle L, Decorps M. Methodology of brain perfusion imaging. *J. Magn Reson Imaging* 2001; **13**(4): 496–520.
11. Wintermark M, Sesay M, Barbier E, Borbely K, Dillon WP, Eastwood JD, Glenn TC, Grandin CB, Pedraza S, Soustiel JF, Nariai T, Zaharchuk G, Caille JM, Dousset V, Yonas H. Comparative overview of brain perfusion imaging techniques. *Stroke* 2005; **36**(9): 2032–2033.
12. Aronen HJ, Gazit IE, Louis DN, Buchbinder BR, Pardo FS, Weisskoff RM, Harsh GR, Cosgrove GR, Halpern EF, Hochberg FH. Cerebral blood volume maps of gliomas: comparison with tumor grade and histologic findings. *Radiology* 1994; **191**(1): 41–51.
13. Maeda M, Itoh S, Kimura H, Iwasaki T, Hayashi N, Yamamoto K, Ishii Y, Kubota T. Tumor vascularity in the brain: evaluation with dynamic susceptibility-contrast MR imaging. *Radiology* 1993; **189**(1): 233–238.
14. Schmainda KM, Rand SD, Joseph AM, Lund R, Ward BD, Pathak AP, Ulmer JL, Badruddoja MA, Krouwer HG. Characterization of a first-pass gradient-echo spin-echo method to predict brain tumor grade and angiogenesis. *AJNR Am J Neuroradiol* 2004; **25**(9): 1524–1532.
15. Donahue KM, Krouwer HG, Rand SD, Pathak AP, Marszalkowski CS, Censky SC, Prost RW. Utility of simultaneously acquired gradient-echo and spin-echo cerebral blood volume and morphology maps in brain tumor patients. *Magn Reson Med* 2000; **43**(6): 845–853.
16. Tropres I, Grimault S, Vaeth A, Grillon E, Julien C, Payen JF, Lamalle L, Decorps M. Vessel size imaging. *Magn Reson Med* 2001; **45**(3): 397–408.
17. Pathak AP, Schmainda KM, Ward BD, Linderman JR, Rebro KJ, Greene AS. MR-derived cerebral blood volume maps: issues regarding histological validation and assessment of tumor angiogenesis. *Magn Reson Med* 2001; **46**(4): 735–747.

18. Pathak AP, Rand SD, Schmainda KM. The effect of brain tumor angiogenesis on the in vivo relationship between the gradient-echo relaxation rate change (DeltaR2*) and contrast agent (MION) dose. *J. Magn Reson Imaging* 2003; **18**(4): 397–403.
19. Tropres I, Lamalle L, Peoc'h M, Farion R, Usson Y, Decorps M, Remy C. In vivo assessment of tumoral angiogenesis. *Magn Reson Med* 2004; **51**(3): 533–541.
20. Kiselev VG, Strecker R, Ziyeh S, Speck O, Hennig J. Vessel size imaging in humans. *Magn Reson Med* 2005; **53**(3): 553–563.
21. Dennie J, Mandeville JB, Boxerman JL, Packard SD, Rosen BR, Weisskoff RM. NMR imaging of changes in vascular morphology due to tumor angiogenesis. *Magn Reson Med* 1998; **40**(6): 793–799.
22. Ferretti S, Allegrini PR, O'Reilly T, Schnell C, Stumm M, Wartmann M, Wood J, McSheehy PM. Patupilone induced vascular disruption in orthotopic rodent tumor models detected by magnetic resonance imaging and interstitial fluid pressure. *Clin Cancer Res* 2005; **11**(21): 7773–7784.
23. Batchelor TT, Sorensen AG, di TE, Zhang WT, Duda DG, Cohen KS, Kozak KR, Cahill DP, Chen PJ, Zhu M, Ancukiewicz M, Mrugala MM, Plotkin S, Drappatz J, Louis DN, Ivy P, Scadden DT, Benner T, Loeffler JS, Wen PY, Jain RK. AZD2171, a pan-VEGF receptor tyrosine kinase inhibitor, normalizes tumor vasculature and alleviates edema in glioblastoma patients. *Cancer Cell* 2007; **11**(1): 83–95.
24. Barth RF. Rat brain tumor models in experimental neuro-oncology: the 9L, C6, T9, F98, RG2 (D74), RT-2 and CNS-1 gliomas. *J. Neurooncol* 1998; **36**(1): 91–102.
25. Valable S, Barbier EL, Bernaudin M, Roussel S, Segebarth C, Petit E, Remy C. In vivo MRI tracking of exogenous monocytes/macrophages targeting brain tumors in a rat model of glioma. *Neuroimage* 2007; **37 Suppl 1**: S47–S58.
26. Benda P, Someda K, Messer J, Sweet WH. Morphological and immunochemical studies of rat glial tumors and clonal strains propagated in culture. *J. Neurosurg* 1971; **34**(3): 310–323.
27. Grobben B, De Deyn PP, Slegers H. Rat C6 glioma as experimental model system for the study of glioblastoma growth and invasion. *Cell Tissue Res* 2002; **310**(3): 257–270.
28. Swenberg JA, Koestner A, Wechsler W, Denlinger RH. Quantitative aspects of transplacental tumor induction with ethylnitrosourea in rats. *Cancer Res* 1972; **32**(12): 2656–2660.
29. Deichmann R, Schwarzbauer C, Turner R. Optimisation of the 3D MDEFT sequence for anatomical brain imaging: technical implications at 1.5 and 3 T. *Neuroimage* 2004; **21**(2): 757–767.
30. Tofts PS, Brix G, Buckley DL, Evelhoch JL, Henderson E, Knopp MV, Larsson HB, Lee TY, Mayr NA, Parker GJ, Port RE, Taylor J, Weisskoff RM. Estimating kinetic parameters from dynamic contrast-enhanced T(1)-weighted MRI of a diffusable tracer: standardized quantities and symbols. *J. Magn Reson Imaging* 1999; **10**(3): 223–232.
31. Meiboom S, Gill D. Modifed Spin Echo method of measuring nuclear relaxation times. *Rev Sci Instrum* 1958; **29**(8): 688–691.
32. Valable S, Montaner J, Bellail A, Berezowski V, Brillault J, Cecchelli R, Divoux D, Mackenzie ET, Bernaudin M, Roussel S, Petit E. VEGF-induced BBB permeability is associated with an MMP-9 activity increase in cerebral ischemia: both effects decreased by Ang-1. *J. Cereb Blood Flow Metab* 2005; **25**(11): 1491–1504.
33. Fross RD, Warnke PC, Groothuis DR. Blood flow and blood-to-tissue transport in 9L gliosarcomas: the role of the brain tumor model in drug delivery research. *J. Neurooncol* 1991; **11**(3): 185–197.
34. Kalber TL, Smith CJ, Howe FA, Griffiths JR, Ryan AJ, Waterton JC, Robinson SP. A longitudinal study of R2* and R2 magnetic resonance imaging relaxation rate measurements in murine liver after a single administration of 3 different iron oxide-based contrast agents. *Invest Radiol* 2005; **40**(12): 784–791.
35. Moore A, Marecos E, Bogdanov A, Jr, Weissleder R. Tumoral distribution of long-circulating dextran-coated iron oxide nanoparticles in a rodent model. *Radiology* 2000; **214**(2): 568–574.
36. Simonetti AW, Elezi VA, Farion R, Malandain G, Segebarth C, Remy C, Barbier EL. A low temperature embedding and section registration strategy for 3D image reconstruction of the rat brain from autoradiographic sections. *J. Neurosci Methods* 2006; **158**(2): 242–250.
37. Kostourou V, Robinson SP, Whitley GS, Griffiths JR. Effects of overexpression of dimethylarginine dimethylaminohydrolase on tumor angiogenesis assessed by susceptibility magnetic resonance imaging. *Cancer Res* 2003; **63**(16): 4960–4966.
38. Neeman M, Dafni H. Structural, functional, and molecular MR imaging of the microvasculature. *Annu Rev Biomed Eng* 2003; **5**: 29–56.
39. Pathak AP, Ward BD, Schmainda KM. A novel technique for modeling susceptibility-based contrast mechanisms for arbitrary microvascular geometries: the finite perturber method. *Neuroimage* 2008; **40**(3): 1130–1143.
40. Leenders WP, Kusters B, Verrijp K, Maass C, Wesseling P, Heerschap A, Ruiter D, Ryan A, de WR. Antiangiogenic therapy of cerebral melanoma metastases results in sustained tumor progression via vessel co-option. *Clin Cancer Res* 2004; **10**(18 Pt 1): 6222–6230.
41. Sakariassen PO, Prestegarden L, Wang J, Skaftnesmo KO, Mahesparan R, Molthoff C, Sminia P, Sundlisaeter E, Misra A, Tysnes BB, Chekenya M, Peters H, Lende G, Kalland KH, Oyan AM, Petersen K, Jonassen I, van der KA, Feuerstein BG, Terzis AJ, Bjerkvig R, Enger PO. Angiogenesis-independent tumor growth mediated by stem-like cancer cells. *Proc Natl Acad Sci USA* 2006; **103**(44): 16466–16471.
42. Hoehn-Berlage M, Eis M, Back T, Kohno K, Yamashita K. Changes of relaxation times (T1, T2) and apparent diffusion coefficient after permanent middle cerebral artery occlusion in the rat: temporal evolution, regional extent, and comparison with histology. *Magn Reson Med* 1995; **34**(6): 824–834.
43. Barbier EL, Liu L, Grillon E, Payen JF, Lebas JF, Segebarth C, Remy C. Focal brain ischemia in rat: acute changes in brain tissue T1 reflect acute increase in brain tissue water content. *NMR Biomed* 2005; **18**(8): 499–506.
44. Broux C, Tropres I, Montigon O, Julien C, Decorps M, Payen JF. The effects of sustained hyperventilation on regional cerebral blood volume in thiopental-anesthetized rats. *Anesth Analg* 2002; **95**(6): 1746–1751.
45. Julien C, Payen JF, Tropres I, Farion R, Grillon E, Montigon O, Remy C. Assessment of vascular reactivity in rat brain glioma by measuring regional blood volume during graded hypoxic hypoxia. *Br J Cancer* 2004; **91**(2): 374–380.
46. Fan G, Zang P, Jing F, Wu Z, Guo Q. Usefulness of diffusion/perfusion-weighted MRI in rat gliomas: correlation with histopathology. *Acad Radiol* 2005; **12**(5): 640–651.
47. Hayashida Y, Hirai T, Morishita S, Kitajima M, Murakami R, Korogi Y, Makino K, Nakamura H, Ikushima I, Yamura M, Kochi M, Kuratsu JI, Yamashita Y. Diffusion-weighted imaging of metastatic brain tumors: comparison with histologic type and tumor cellularity. *AJNR Am J Neuroradiol* 2006; **27**(7): 1419–1425.
48. Kimura R, Nakase H, Tamaki R, Sakaki T. Vascular endothelial growth factor antagonist reduces brain edema formation and venous infarction. *Stroke* 2005; **36**(6): 1259–1263.
49. Uehara H, Miyagawa T, Tjuvajev J, Joshi R, Beattie B, Oku T, Finn R, Blasberg R. Imaging experimental brain tumors with 1-aminocyclopentane carboxylic acid and alpha-amino-isobutyric acid: comparison to fluorodeoxyglucose and diethylenetriaminepentaacetic acid in morphologically defined tumor regions. *J. Cereb Blood Flow Metab* 1997; **17**(11): 1239–1253.
50. Inamura T, Black KL. Bradykinin selectively opens blood-tumor barrier in experimental brain tumors. *J. Cereb Blood Flow Metab* 1994; **14**(5): 862–870.
51. Seitz RJ, Deckert M, Wechsler W. Vascularization of syngenic intracerebral RG2 and F98 rat transplantation tumors. A. histochemical and morphometric study by use of ricinus communis agglutinin I. *Acta Neuropathol (Berl)* 1988; **76**(6): 599–605.
52. Schlageter KE, Molnar P, Lapin GD, Groothuis DR. Microvessel organization and structure in experimental brain tumors: microvessel populations with distinctive structural and functional properties. *Microvasc Res* 1999; **58**(3): 312–328.

DOI: 10.1002/nbm

53. Farrell CL, Farrell CR, Stewart PA, Del Maestro RF, Ellis CG. The functional microcirculation in a glioma model. *Int J Radiat Biol* 1991; **60**(1–2): 131–137.
54. Holash J, Maisonpierre PC, Compton D, Boland P, Alexander CR, Zagzag D, Yancopoulos GD, Wiegand SJ. Vessel cooption, regression, and growth in tumors mediated by angiopoietins and VEGF. *Science* 1999; **284**(5422): 1994–1998.
55. Maisonpierre PC, Suri C, Jones PF, Bartunkova S, Wiegand SJ, Radziejewski C, Compton D, McClain J, Aldrich TH, Papadopoulos N, Daly TJ, Davis S, Sato TN, Yancopoulos GD. Angiopoietin-2, a natural antagonist for Tie2 that disrupts in vivo angiogenesis. *Science* 1997; **277**(5322): 55–60.
56. Hu B, Guo P, Fang Q, Tao HQ, Wang D, Nagane M, Huang HJ, Gunji Y, Nishikawa R, Alitalo K, Cavenee WK, Cheng SY. Angiopoietin-2 induces human glioma invasion through the activation of matrix metalloprotease-2. *Proc Natl Acad Sci USA* 2003; **100**(15): 8904–8909.
57. Galis ZS, Khatri JJ. Matrix metalloproteinases in vascular remodeling and atherogenesis: the good, the bad, and the ugly. *Circ Res* 2002; **90**(3): 251–262.

DOI: 10.1002/nbm